

Role of AGNs in the Luminous Infrared Galaxy phase since $z \sim 3$

Ming-Yi Lin^{1,2,*}, Yasuhiro Hashimoto² and Sébastien Foucaud^{3,4,2}

¹Max-Planck-Institut für Extraterrestrische Physik (MPE), Giessenbachstrasse 1, 85748 Garching, Germany

²Department of Earth Sciences, National Taiwan Normal University, No.88, Tingzhou Road, Sec. 4, Taipei 11677, Taiwan

³Center for Astronomy & Astrophysics, Department of Physics & Astronomy, Shanghai JiaoTong University, 800 Dongchuan Road, Shanghai 200240, China

⁴Institute of Astronomy and Astrophysics, Academia Sinica, P.O. Box 23-14, Taipei 10617, Taiwan

Accepted 2015 November 20. Received 2015 November 19; in original form 2013 January 12

ABSTRACT

In order to understand the interactions between active galactic nuclei (AGN) and star formation during the evolution of galaxies, we investigate 142 galaxies detected in both X-ray and $70\mu\text{m}$ observations in the COSMOS (Cosmic Evolution Survey) field. All of our data are obtained from the archive, X-ray point source catalogs from Chandra and XMM-Newton observations; far-infrared $70\mu\text{m}$ point source catalog from Spitzer-MIPS observations. Although the IRAC $[3.6\mu\text{m}]-[4.5\mu\text{m}]$ vs. $[5.8\mu\text{m}]-[8.0\mu\text{m}]$ colours of our sample indicate that only $\sim 63\%$ of our sources would be classified as AGN, the ratio of the rest-frame 2–10 keV luminosity to the total infrared luminosity ($8\text{--}1000\mu\text{m}$) shows that all of the sample has comparatively higher X-ray luminosity than that expected from pure star-forming galaxies, suggesting the presence of an AGN in all of our sources. From the analysis of the X-ray hardness ratio, we find that sources with both $70\mu\text{m}$ and X-ray detection tend to have a higher hardness ratio relative to the whole X-ray selected source population, suggesting the presence of more X-ray absorption in the $70\mu\text{m}$ detected sources. In addition, we find that the observed far-infrared colours of $70\mu\text{m}$ detected sources with and without X-ray emission are similar, suggesting the far-infrared emission could be mainly powered by star formation.

Key words: galaxies: high-redshift – galaxies: active – infrared: galaxies – X-rays: galaxies.

1 INTRODUCTION

Observational and theoretical evidences over the past decades strongly suggest the existence of supermassive black hole (SMBH) within the spherical bulge of galaxies. The tight connection between the SMBH mass and bulge properties, such as bulge luminosity or stellar velocity dispersion, indicates a scenario of co-evolution of central black hole and its host galaxy (Kormendy & Richstone 1995; Magorrian et al. 1998). Galaxy merger is a plausible interpretation to explain the concomitant growth of black hole and host galaxy under the Λ CDM model (Treister et al. 2010). As tidal effects distort the morphology of galaxies during mergers, episodes of extreme star formation can occur; therefore interstellar medium (ISM) is abundantly produced, either from supernova explosions or stellar wind of evolved stars. Accompanying this morphological effect, merger not only reduces angular momentum but also induces gas accumulation around circumnuclear region (Barnes & Hernquist 1991). The large amount of dust and molecular gas around the central region funnels onto the SMBH in the galactic nucleus and consequently triggers a phase of active galactic nuclei (AGNs), with its powerful electromagnetic radiation spanning from radio to gamma-ray. In the later galaxy

evolution stages, the merger scenario implies that the radiation-pressure or kinematic-wind feedback from AGN may quench the star formation, expelling the remnant gas and dust. At the same time, central AGN turns into an optically unobscured quasar, a class of luminous AGN. Final outcome of the galaxy evolution is a red elliptical galaxy (Hopkins et al. 2008, and references therein).

Sanders et al. (1988a) first proposed a connection between the Ultra Luminous Infrared Galaxies (ULIRGs; $L_{\text{IR}} \geq 10^{12} L_{\odot}$) and quasars as two successive snapshots of merger event between two gas-rich spiral galaxies. Indeed, the analysis of the IRAS 1 Jy ULIRGs survey revealed a large fraction of interacting galaxies at $z < 0.1$ in favor of such merger-ULIRG scenario (Borne et al. 2000; Cui et al. 2001; Veilleux et al. 2002). Besides, the merger fraction has been shown to increase as infrared luminosity increases, merging galaxies being the prevalent population amongst ULIRGs to redshift $z \sim 1$ (Shi et al. 2009). However at higher redshift $z \sim 2$, the merging galaxy fraction drops slightly and non-interacting disk galaxy fraction increases (Kartaltepe et al. 2012). On the other hand, the merger-AGN connection is more difficult to observe. Although, in the local universe, optical luminous quasars are considered to be related to post-starburst mergers (Canalizo & Stockton 2001; Bennert et al. 2008); at $1.5 < z < 2.5$, AGNs are more likely to occur inside of normal disk or bulge galaxies instead of interacting systems, suggesting that secular pro-

*E-mail: 699440083@ntnu.edu.tw, mingyi@mpe.mpg.de

cesses (such as bars or nucleus rings) may trigger nuclear activity instead of major-merger (Schawinski et al. 2011; Kocevski et al. 2012). The connection between ULIRGs and AGNs has been investigated for the past few years. The AGN fraction seems to rise with increasing infrared luminosity (Genzel & Cesarsky 2000; Kartaltepe et al. 2010) as the AGN activity likely influences the host galaxy infrared spectral energy distribution (SED). Galaxies with higher mid-infrared flux ratio (i.e. $F_{25}/F_{60} \geq 0.2$) may be classified as warm ULIRGs, which are supposed to be dominated by AGN. Galaxies with lower mid-infrared flux ratio (i.e. $F_{25}/F_{60} \leq 0.2$) may be classified as cold ULIRGs, which are supposed to be dominated by star formation (Sanders et al. 1988b; Veilleux et al. 2009).

In order to determine the exact role of the AGN in the overall galaxy evolution, it is essential to separate the AGN contribution from the star formation activity. To decouple these two components, three distinct methods can be used:

(i) *Specific emission lines ratio* - Fine structure radiation in optical and infrared wavelength are reliable tracers of excitation state of the ISM in galaxies. A classification based on two independent line ratios can help to distinguish AGN from star forming galaxies. For instance, it is possible to separate the main mechanism responsible for the excitation of the gas, between normal HII regions, objects photoionized by AGN, and shockwave heating by star formation, using $[\text{OIII}]\lambda 5007\text{\AA}/\text{H}\beta$ versus $[\text{NII}]\lambda 6584\text{\AA}/\text{H}\alpha$ diagram (Baldwin et al. 1981, BPT). Unfortunately, galaxy mergers suffer from dust obscuration, especially at optical wavelengths, reducing the efficiency of such diagnostics; although a complete misclassification of AGN is unlikely (Veilleux 2002; LaMassa et al. 2012).

With the advent of the infrared spectrometer on the Infrared Space Observatory (ISO) and the Spitzer telescope, other emission lines were identified for AGN diagnostics in the mid-infrared with less extinction. For example, the line ratio $[\text{O IV}]\lambda 25.9\mu\text{m}/[\text{NeII}]\lambda 12.8\mu\text{m}$ or $[\text{NeV}]\lambda 14.3\mu\text{m}/[\text{NeII}]\lambda 12.8\mu\text{m}$ is a reliable indicator to separate AGNs from star-forming galaxies (Genzel et al. 1998; Armus 2006). The different Polycyclic Aromatic Hydrocarbon (PAH) emission features at $6.2\mu\text{m}$, $7.7\mu\text{m}$ and $11.3\mu\text{m}$ are other reliable star formation tracers, with weaker PAH emission corresponding to higher AGN contribution (Voit 1992; Veilleux et al. 2009);

(ii) *Continuum slope* - The cold dust emission in the far-infrared band is mainly due to star formation. In contrast, hot dust components around $10\mu\text{m}$ are considered to be associated with AGN activity. As the influence of the AGN becomes significant in the galaxy, the infrared spectral indexes start to be dominated by a power-law continuum $\sim 10\mu\text{m}$ (Alonso-Herrero et al. 2006; Donley et al. 2007). Therefore, the mid-infrared to far-infrared ratio is a simple measure to quantify the relative contributions of AGN and star formation (Veilleux et al. 2009);

(iii) *Spectral energy distribution fitting* - With the development of deep multi-wavelength photometric surveys, panchromatic SED studies are becoming increasingly popular. Theoretical or empirical templates are commonly used to fit the SED and determine the photometric redshifts of galaxies. Multi-component fitting, including the contribution from stars, dust, and AGNs is now possible due to very broad photometric coverage. In the case of heavily obscured AGNs, although star formation of host galaxy dominates the flux at most wavelengths, a bump in mid-infrared produced by the circumnuclear dust radiation can be an indicator of an obscured AGN. Therefore, identifying hot dust component from the galaxy

SED is a reliable way to determine the AGN contribution to total infrared luminosity (Mullaney et al. 2011; Pozzi et al. 2012).

Although the different methods may not agree completely on defining a pure sample (i.e. pure-AGN or pure starburst galaxy), they all provide evidences that, for the major part of the samples, AGN and star formation occur concomitantly. What is essential then is to understand the mutual influence on the properties of AGNs and their host star-forming galaxies. We try to understand whether the dust and gas from star formation in host galaxy could obscure central AGN or the presence of AGN radiation could change the far-infrared SED.

The SEDs of Luminous Infrared Galaxies (LIRGs; $10^{11} L_{\odot} \leq L_{\text{IR}} < 10^{12} L_{\odot}$) and ULIRGs peak in the range of $40\text{--}200\mu\text{m}$ (Sanders & Mirabel 1996). In fact, the $70\mu\text{m}$ Spitzer band is ideal to unambiguously trace star-forming galaxies in the local universe as it is little affected by PAH features, silicate feature, and stellar flux. Central AGNs are usually identified by their strong X-ray continuum emission. Indeed, high energy X-ray photons emitted by hot corona of accretion disk (e.g., Haardt & Maraschi 1993) around the central black hole are usually less absorbed by dust and gas from host galaxies compared to lower energy UV-photons. One noticeable exception is Compton thick objects ($N_H > 10^{24} \text{ cm}^{-2}$) for which even hard X-ray photons are absorbed. Compton-thick AGNs are not an uncommon occurrence among ULIRG population. The detection of Fe $K\alpha$ lines and large amount of neutral hydrogen absorption in hard X-ray spectrum support the presence of Compton-thick AGN inside ULIRG (e.g. Mrk 273 in Balestra et al. (2005) paper).

Several studies have investigated the nature of the $70\mu\text{m}$ galaxy population. Patel et al. (2011) led a spectroscopic follow-up in optical wavelength of $70\mu\text{m}$ galaxies selected from the Spitzer Wide-area Infrared Extragalactic (SWIRE) Legacy Survey. Their results suggest that, for galaxies not dominated by QSO, most of the IR photons are emitted by star-forming regions, while contribution of emission by AGN dusty torus is negligible. Furthermore, Symeonidis et al. (2010) investigated the SEDs of 61 $70\mu\text{m}$ -selected galaxies from the 0.5 deg^2 wide Extended Groth Strip (EGS) field and concluded that, even for galaxies displaying powerful hard X-ray emission originating from AGNs, cold dust emission templates are still required to explain the observed strong far-infrared luminosity. To reveal a potential starburst-AGN connection, Trichas et al. (2009) used 28 X-ray sources with $70\mu\text{m}$ detection and applied a statistical Kolmogorov-Smirnov test (K-S test) to assess any difference in hardness ratio between $70\mu\text{m}$ detected X-ray galaxies and the whole X-ray population in the redshift interval $0.5 < z < 1.3$. However, the K-S test shows a none significant probability, in contrast to the prediction of AGN/starburst co-evolution models (Hopkins et al. 2008).

In this paper, we will unveil the role of AGN in the infrared (ultra)luminous phase of galaxy evolution by comparing the properties of an X-ray detected subsample and its parent $70\mu\text{m}$ -selected sample. Our main $70\mu\text{m}$ galaxy catalog was published by Kartaltepe et al. (2010), which includes total infrared luminosity, multi-wavelength photometry and redshift. We describe the data used for this work in section 2. As we are interested in the physical properties of AGN and their far-infrared selected host galaxy, we have to cross-match X-ray and $70\mu\text{m}$ datasets. In section 3, we depict our matching method as well as the methods used to estimate and calibrate different physical parameter measurements. We present our results in section 4, and engage in detailed discussions in section 5. Throughout this paper, we adopt a standard cosmological model with the following parameters: $H_0 = 70 \text{ km s}^{-1} \text{ Mpc}^{-1}$,

and $\Omega_M = 0.3$, $\Omega_\Lambda = 0.7$. Unless otherwise stated, all magnitudes in this paper are in the Vega system.

2 DATA

The Cosmic Evolution Survey (COSMOS) is the largest Treasury program using Hubble Space Telescope imaging a ~ 2 deg²-wide equatorial field in the optical F814W filter (approximately corresponds to I band) with the Advanced Camera for Surveys (ACS) instrument (Scoville et al. 2007a,b; Koekemoer et al. 2007). Several large follow-up campaigns using ground-based and space-based telescopes have produced a comprehensive photometric and spectroscopic dataset across a whole spectrum (Capak et al. 2007; Hasinger et al. 2007; Sanders et al. 2007; Scott et al. 2008)¹. Kartaltepe et al. (2010) published a reliable 70 μ m selected galaxy sample (1503 sources) with signal-to-noise (S/N) > 3 from Spitzer data in the COSMOS field and provided their corresponding redshift, total infrared luminosity, and multi-wavelength photometry. In this study, we attempt to find the X-ray counterparts of 70 μ m selected galaxies. We use both XMM-Newton and Chandra observations in the COSMOS field, taking advantage of the wider observational field of the XMM-Newton survey and the deeper observational depth of the Chandra survey to maximize the total number of X-ray point source counterparts in the 70 μ m selected galaxy sample. In the following subsections, we will give a brief description of infrared and X-ray datasets.

2.1 Spitzer-COSMOS

Spitzer-COSMOS (S-COSMOS) is a Legacy program designed to cover the COSMOS field with deep Spitzer observations in IRAC four bands (i.e. 3.6, 4.5, 5.8, and 8.0 μ m) and MIPS three bands (i.e. 24, 70, and 160 μ m). The initial Cycle 2 program conducted in 2006 consisted of a deep IRAC survey and a narrow-field MIPS survey. The total integration time of the deep IRAC survey is 166 hours, reaching 5σ sensitivities of 0.9, 1.7, 11.3, and 14.6 μ Jy, in 3.6, 4.5, 5.8, and 8.0 μ m band, respectively (Sanders et al. 2007). A complementary MIPS deep observation of 450 hours has been conducted in Cycle 3 ensuring accurate 70 and 160 μ m flux density measurements. The median exposure times were ~ 3400 s, 1350s, and 270s for 24 μ m, 70 μ m, and 160 μ m bands, respectively, corresponding to 5σ depths of ~ 0.08 , 8.5, and 65 mJy (Le Floch et al. 2009; Frayer et al. 2009; Kartaltepe et al. 2010).

2.2 X-ray dataset: XMM-Newton & Chandra

The COSMOS field has been covered with observations from both XMM-Newton (XMM) and Chandra observatories.

A 2 deg² contiguous survey has been conducted with XMM to reach medium depth (~ 60 ks). COSMOS X-ray catalog made by XMM observation provides three different energy bands. Based on the logN-logS relationship, the flux limit of 0.5-2 keV (soft band), 2-10 keV (hard band), and 5-10 keV (ultra-hard band) dropped to 7.2×10^{-16} ergs cm⁻² s⁻¹, 4.0×10^{-15} ergs cm⁻² s⁻¹, and 9.7×10^{-15} ergs cm⁻² s⁻¹, respectively (Hasinger et al. 2007;

Cappelluti et al. 2009). In total, 1887 point-like sources were identified in the XMM-COSMOS survey. Brusa et al. (2010) has released a cross matched catalog between these sources and optical counterparts (I band, catalog of Capak et al. (2007)), providing redshifts (spectroscopic and photometric), UV to 24 μ m photometry, and hardness ratio.

The Chandra-COSMOS (C-COSMOS) Survey images a ~ 0.9 deg² field in the central part of the original COSMOS field, with the effective exposure time ~ 160 ks in center 0.5 deg² and ~ 80 ks in outer 0.4 deg². C-COSMOS catalog provides three different energy bands, 0.5-2 keV (soft band), 2-7 keV (hard band), and 0.5-7 keV (full band), with corresponding flux limits of 1.9×10^{-16} ergs cm⁻² s⁻¹, 7.3×10^{-16} ergs cm⁻² s⁻¹, and 5.7×10^{-16} ergs cm⁻² s⁻¹, respectively. In total, 1761 point-like sources have been extracted in the in C-COSMOS field (Elvis et al. 2009).

3 METHOD

3.1 Matched X-ray and far-infrared point source catalog

The spatial resolution of the Spitzer Telescope at 70 μ m is around 18'', much larger than the spatial resolution of XMM or Chandra X-ray observatory. Therefore, it is crucial to accurately detect the position of the 70 μ m galaxies. Kartaltepe et al. (2010) have identified 1503 optical or near-IR counterpart to the 70 μ m selected galaxies. We take advantage of the Altas resource from IRSA/COSMOS archive² to match the optically or near-IR identified counterparts of 70 μ m selected galaxies with the XMM and Chandra point source catalogs, separately. We independently match 108 and 92 of our 70 μ m-selected galaxies with counterparts from the XMM and the Chandra catalogs, using searching radii of 3'' and 1'', respectively. The searching radii are defined by the 90% completeness of X-ray-to-Optical position offset distribution (c.f. upper panel in Figure 3 of Brusa et al. (2007) for XMM-COSMOS sample; Figure 6 of Elvis et al. (2009) for C-COSMOS). The median angular distances between the position of the X-ray source and the position of optical/near-IR identified counterpart of our 70 μ m-selected galaxies are 0.9'' and 0.3'' for the XMM and Chandra point source catalogs, respectively. 58 sources are identified in both X-ray catalogs, and a total number of 142 galaxies are assigned to both 70 μ m and X-ray measurements in the COSMOS field. We will refer to this sample as "70 μ m/X-ray" galaxy catalog in the remaining part of this article. From the same datasets, Kartaltepe et al. (2010) had identified 154 X-ray detected 70 μ m galaxies (refer to Figure 7 in their paper). The 12 extra objects compared to our own matched catalog resulted from a slightly less strict matching criterion used by Kartaltepe et al. (2010). We speculate that these additional sources are more distant from the 70 μ m source position. The number of sources from our different catalogs and matched catalogs are summarized in Table 1.

3.2 Redshift determination and total infrared luminosity

Several spectroscopic surveys were conducted to measure the redshifts of galaxies in the COSMOS field. The most extensive survey in this field is the zCOSMOS survey (Lilly et al. 2007), a

¹ c.f. the COSMOS Special Issue of the Astrophysical Journal Supplement Series, in September, 2007.

² NASA/IPAC infrared service archive of COSMOS project. <http://irsa.ipac.caltech.edu/data/COSMOS>

Table 1. Samples properties and matching results

Catalog	Area ^(a) in deg ²	Flux limits ^(b) in mJy ^(†) or 10 ⁻¹⁶ ergs cm ⁻² s ⁻¹ ^(‡)	N_S ^(c)	$N_{70\mu\text{m}}$ ^(d)	References ^(e)
Spitzer-COSMOS (S-COSMOS) 70 μm galaxies catalog	2.47	8.5 ^(†) (5 σ)	1503	1503	Frayser et al. (2009) & Kartaltepe et al. (2010)
XMM-COSMOS Point source catalog	2.13	7.2 ^(‡) (Soft band) 40 ^(‡) (Hard band) 97 ^(‡) (Ultra hard band)	1797	108	Cappelluti et al. (2009) & Brusa et al. (2010)
Chandra-COSMOS (C-COSMOS) Point source catalog	0.9 ^(f)	1.9 ^(‡) (Soft band) 7.3 ^(‡) (Hard band) 5.7 ^(‡) (Full band)	1761	92	Elvis et al. (2009)
XMM- & Chandra-COSMOS concatenated catalog ^(g)	0.9 ^(h)	–	2821	142	This work

^(a)Effective area covered by the survey; ^(b) Flux limit of the catalog; ^(c)Total number of sources; ^(d)Number of sources cross-matched with the 70 μm catalog; ^(e)References describing the catalog; ^(f) central 0.5 deeper; ^(g) Catalog concatenated from XMM- and Chandra-catalogs; sources matched between the two catalogs are not duplicated; the cross-match between this catalog and the 70 μm catalog constitute our primary "70 μm /X-ray" catalog; ^(h)Note that the sky coverage of C-COSMOS is included in the XMM-COSMOS sky coverage.

deep spectroscopic survey conducted with the VLT-VIMOS multi-object spectrograph to study the evolution of faint/obscured galaxies through direct analysis of their emission lines. Although the observations enable us to probe properties of faint objects, only the central 1 deg² is covered by zCOSMOS. Forty-nine of our 70 μm /X-ray galaxies have their redshifts confirmed spectroscopically by zCOSMOS. Observations using other facilities have been conducted on this field providing precise redshifts for fifty-three additional 70 μm /X-ray galaxies (Abazajian et al. 2009; Trump et al. 2007; Kartaltepe et al. 2010; Prescott et al. 2006). In total 102/142 (72%) galaxies with X-ray and 70 μm detection have spectroscopic redshift. Table 2 summarizes the origin and number of our targets with spectroscopic redshifts.

For the remaining galaxies, we use the photometric redshift catalogs built for both non-AGN sources and XMM-selected sources (Ilbert et al. 2009; Salvato et al. 2009) using the publicly available software Le PHARE³ (Arnouts et al. 1999; Ilbert et al. 2006). The 70 μm /X-ray galaxies that do not have spectroscopic redshift have been assigned a photometric redshift (40 out of 142 - 28%).

We use the overlap between our spectroscopic and photometric redshift samples to investigate the quality of the later. The relation between photometric and spectroscopic redshift of 70 μm /X-ray galaxies presents no bias and is comparable to overall 70 μm galaxy with a scatter of $\sigma_z = 0.02 \times (1 + z)$ (Kartaltepe et al. 2010). Bright sources have usually been assigned a spectroscopic redshift, with small error, while faint sources have been assigned a photometric redshift with larger error. Incidentally, even though these two different methods for redshift measurement have different error sizes, the infrared and X-ray luminosity distribution inferred both by spectroscopically and photometrically determined redshifts have the same median value. Therefore, we conclude the difference in redshift measurements does not induce any systematic bias.

Kartaltepe et al. (2010) used Spitzer-MIPS (24, 70, 160 μm) data points to estimate the total infrared luminosity (L_{IR}) for 70 μm selected galaxies by fitting the SEDs with a χ^2 -minimization

Table 2. Confirmed spectroscopic redshift sample

Telescope	Instrument	$N^{(a)}$	Reference
ESO-VLT	VIMOS	49	zCOSMOS Lilly et al. (2007)
Magellan	IMACS	26	Trump et al. (2007)
Sloan	SDSS	15	Abazajian et al. (2009)
Keck II	DEIMOS	11	Kartaltepe et al. (2010)
MMT	Hectospec	1	Prescott et al. (2006)

^(a)Number of 70 μm /X-ray sources with spectroscopic redshift.

method using the Le PHARE³ SED fitting code and integrating the luminosity over the 8-1000 μm wavelength range. Four infrared libraries have been used, including the SEDs of local star-forming galaxies and SEDs derived from radiative transfer models. The details are described in Sec. 4.2 of Kartaltepe et al. (2010). However, this catalog suffers from incompleteness in the 160 μm band and lacks any direct photometric observation in the Rayleigh-Jeans part of the SED. There are 463 70 μm sources with 160 μm detections (463 out of 1503; 31%), and most of them (417 out of 463; 89%) have a single matched 160 μm source within the given MIPS error circle. For the 160 μm sources with multiple 70 μm counterparts, Kartaltepe et al. (2010) assigned the brightest 70 μm source as the counterpart of the 160 μm source. Kartaltepe et al. (2010) assessed that measurements of L_{IR} without 160 μm data are underestimated by 0.2 dex compared to measurements with 160 μm data. Despite these caveats, we assume that this catalog is robust enough for our study, as the galaxies without 160 μm photometry are equally spread between the samples of 70 μm galaxies with or without X-ray detections. Another caveat in this catalog is that the SED fitting does not take into account any AGN contribution at mid-infrared wavelengths. Therefore, for those 70 μm galaxies having a significant contribution from an AGN hot dust component over 5-30 μm , L_{IR} may be contaminated by AGN emission. Since the SED of the hot dust itself drops dramatically beyond 30 μm (Lusso et al. 2013), the AGN contribution to 8-1000 μm emission is likely to be small. Other studies have investigated this issue, e.g., Pozzi et al. (2012) used luminous infrared galaxies at $z \sim 2$ with Herschel observations

³ <http://www.cfht.hawaii.edu/~arnouts/LEPHARE>

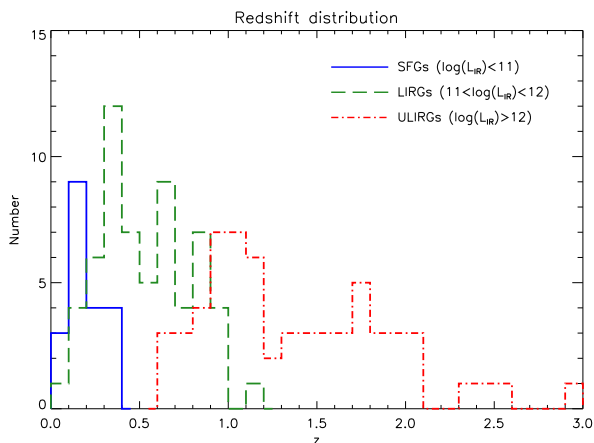


Figure 1. The redshift distribution of $70\mu\text{m}/\text{X-ray}$ galaxies. We divide our total sample into three distinct classes according to their total infrared luminosity: star-forming galaxies (SFGs; $L_{\text{IR}} < 10^{11} L_{\odot}$; blue solid line) at a median redshift of $z \sim 0.168$, luminous infrared galaxies (LIRGs; $10^{11} L_{\odot} \leq L_{\text{IR}} < 10^{12} L_{\odot}$; green dash line) at $z \sim 0.518$ and ultra-luminous infrared galaxies (ULIRG; $L_{\text{IR}} \geq 10^{12} L_{\odot}$; red dash-dot line) at $z \sim 1.268$.

in the Chandra Deep Field-South (CDF-S) field and concluded that the AGN contribution to $8\text{--}1000\mu\text{m}$ emission is only 5%.

We divide our $70\mu\text{m}/\text{X-ray}$ galaxy sample (142) into three distinct classes, according to their total infrared luminosity as star-forming galaxy (SFG, 20/142), luminous infrared galaxy (LIRG, 60/142), and ultra-luminous infrared galaxy (ULIRG, 62/142) with $L_{\text{IR}} < 10^{11} L_{\odot}$, $10^{11} L_{\odot} \leq L_{\text{IR}} < 10^{12} L_{\odot}$, and $L_{\text{IR}} \geq 10^{12} L_{\odot}$, respectively. Figure 1 shows the redshift distributions in the different infrared luminosity intervals: SFGs with median $z \sim 0.168$, LIRGs with median $z \sim 0.518$, and ULIRGs with median $z \sim 1.268$.

3.3 Correction of X-ray properties

By combining both XMM and Chandra X-ray catalogs, we extend our total sample of $70\mu\text{m}/\text{X-ray}$ galaxies to 142 sources, 58 of which are listed in both X-ray catalogs. The Chandra and XMM catalogs use different energy bands to present hard X-ray count rate: 2-7 keV for Chandra and 2-10 keV for XMM. In both the XMM and Chandra catalogs, the hard X-ray count rate is converted (extrapolated) into the hard X-ray flux at 2-10 keV by assuming a power-law spectrum with spectral index Γ and Galactic column density N_{H} . However, the two catalogs use different assumptions: XMM catalog used $\Gamma = 1.7$ and Galactic column density $N_{\text{H}} = 2.5 \times 10^{20} \text{ cm}^{-2}$ (Cappelluti et al. 2009); Chandra catalog used $\Gamma = 1.4$ and Galactic column density $N_{\text{H}} = 2.7 \times 10^{20} \text{ cm}^{-2}$ (Elvis et al. 2009). Because different assumptions have been applied to the X-ray catalogs, to make two catalogs consistent, we calculate the hard X-ray luminosity conversion equation by fitting a line to the hard X-ray luminosities for the 58 sources with detection in both catalogs. We denote that, in this section, the paired data are fitted to a linear equation ($y = a \times x + b$) by minimum χ^2 method. The measured errors in observational data have been taken into account. The best-fitted linear model parameters [a,b] include the $1\text{-}\sigma$ uncertainties. Figure 2 shows the correlation of hard X-ray luminosity between XMM and Chandra. The hard X-ray luminos-

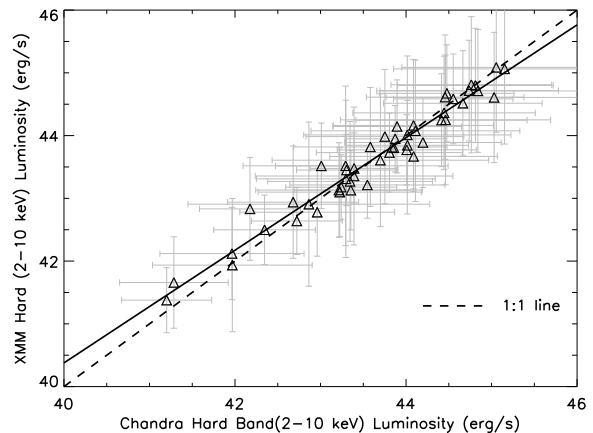


Figure 2. Hard X-ray luminosity from the XMM catalog (Brusa et al. 2010) versus hard X-ray luminosity from the Chandra catalog (Elvis et al. 2009) for our $70\mu\text{m}/\text{X-ray}$ galaxies. A linear fit (see Equation (1)) is shown as the black solid line. The black dash line indicates 1:1 line.

ity conversion equation is:

$$\log(L_{X,XMM}) = 0.9(\pm 0.03) \times \log(L_{X,Chandra}) + 4.46(\pm 1.2) \quad (1)$$

If sources have been observed in the XMM survey, we adopt the hard X-ray luminosity derived from the XMM catalog. For the remaining sources in the Chandra catalog, their hard X-ray luminosity is converted to the XMM band system using Equation (1). The new uncertainty of their hard X-ray luminosity is computed according to the 1σ dispersion of the hard X-ray luminosity conversion equation. *Correcting the systematic difference between the hard X-ray luminosities measured with Chandra and those measured with XMM, is the final step in ensuring that all hard X-ray luminosities are in the XMM band system.*

One of the main goals of our study is to explore the relationship between the host galaxy extinction and the central region obscuration. The X-ray hardness ratio (hereafter HR), defined as $\text{HR} = (\text{H} - \text{S})/(\text{H} + \text{S})$, where H is the photon counts in the X-ray hard band and S is the photon counts in the soft band, is typically used as an indication of source spectral shape. Assuming a primary power-law spectrum, the neutral hydrogen column density can be measured by HR. Unlike the X-ray spectral fitting, which requires relatively good S/N, the HR can be used over a wide range of S/N. Our HR values are extracted from Brusa et al. (2010) for XMM catalog, and Elvis et al. (2009) for Chandra catalog. The difference in hard X-ray energy band between the two set of observations may change the HR values. Therefore, given that our samples overlap, we can fit a line and derive an empirical HR conversion equation. In Figure 3, we compare the HR from XMM and Chandra, for the overlapping 38 sources detected in soft and hard bands with both observatories. The HR conversion equation is:

$$\text{HR}_{XMM} = 1.04(\pm 0.06) \times \text{HR}_{Chandra} - 0.09(\pm 0.02) \quad (2)$$

If sources have been observed in the XMM survey, we adopt the HR derived from XMM catalog. For the remaining sources with HR measurements in the Chandra catalog, these are converted to the XMM band system using Equation (2). The new uncertainty of their HR is computed according to the 1σ dispersion of the HR conversion equation. *Correcting the systematic difference between the HRs measured with Chandra and those measured with XMM,*

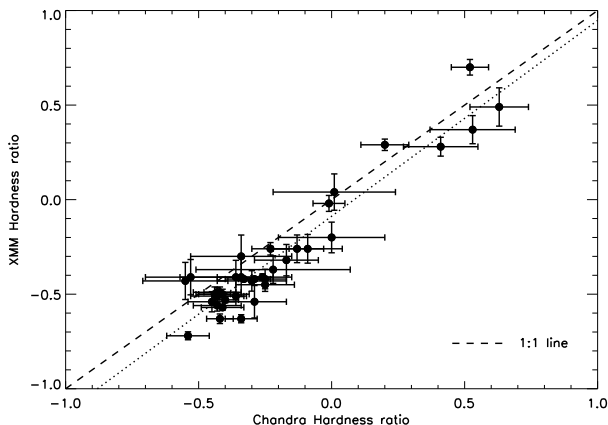


Figure 3. Hardness ratio extracted from the XMM catalog (Brusa et al. 2010) vs. value from the Chandra catalog (Elvis et al. 2009) for our 38 sources detected in soft and hard bands with both observatories. The different hard X-ray energy bands between the two observations influence the hardness ratio measurements. We fit a simple line (dotted line) to estimate a conversion equation between the two different measurements (see Equation (2)). The black dash line indicates 1:1 line.

ensures that all HRs are in the XMM band system. Then, we assume that there are no systematic differences between the HR measurements from both samples. We will later discuss the implication of such assumption in section 4.2. It is worth to remind that time-dependent variability of AGNs (both photon index and flux) can induce stochastic inconsistency in different observations: for instance, Mateos et al. (2007) have summarized that a variation in slope of $\Delta \Gamma \sim 0.2$ could lead to a variation in HR of $\Delta \text{HR} \sim 0.1$.

From our total sample of 142 $70\mu\text{m}/\text{X-ray}$ galaxies, 96 (68%) are detected in both soft and hard X-ray bands. For the remaining 46 (32%) objects, 24 are soft band detection, 21 are hard band detection, and 1 is full band detection (neither detected in soft band nor hard band). We examine the overall L_{IR} and redshift distribution and find no significant difference between these 96 $70\mu\text{m}/\text{X-ray}$ galaxies with measured HRs and the rest of the sample, suggesting that there is no obvious bias within this subsample.

For the purpose of deriving unabsorbed hard X-ray luminosity, we need to correct the neutral hydrogen absorption. We use HR to calculate the column density of neutral hydrogen (N_H). One caveat of such method is that it relies on assumption of a simple absorbed power-law model. Extra components in the source spectra can affect HR measurements, including soft X-ray excess (at 1-2 keV), Fe $K\alpha$ line, and X-ray reflection, which are common in AGN and ULIRG (Teng & Veilleux 2010). These extra components may lead to an underestimation or even prevent to derive an intrinsic N_H . Here, the low X-ray counts of each individual source prevents us to perform X-ray spectrum fitting directly. We therefore use a more uniform and simple procedure to derive a N_H from the HR measurement.

First, we fix the intrinsic photon index of power-law to 1.7 (Wilkes et al. 2005), as a general broad-line AGN. To simulate the observed HR, we use the *Portable, Interactive, Multi-Mission Simulator* (PIMMS)⁴ from HEASARC to model simulated sources with variable amount of N_H covering a redshift interval $0 < z < 3$. Then, by comparing the model HR to the observed HR within a

given redshift, we could obtain our best N_H value. The mean value of HR for $70\mu\text{m}/\text{X-ray}$ galaxies in COSMOS field is -0.16 with corresponding $N_H = 2.7 \times 10^{22} \text{ cm}^{-2}$ (at $z = 0.95$). The bottom panel of Figure 4 shows the N_H distribution of our $70\mu\text{m}/\text{X-ray}$ sample. A caveat of estimating N_H from the HR, is that the HR becomes less sensitive to absorption for high redshift galaxies (e.g. observed-frame 0.5-2 keV shifts to rest-frame 1.5-6 keV at $z = 2$), except for those very heavily obscured AGNs. Therefore, in this study, the N_H of $70\mu\text{m}/\text{X-ray}$ galaxies at high redshift could be unavoidably underestimated.

Then, we apply the best-fitted value of N_H , redshift, and photon index $\Gamma \sim 1.7$ to measure the absorption correction factor between absorbed and unabsorbed hard X-ray luminosity for $70\mu\text{m}/\text{X-ray}$ galaxy. The top panel of Figure 4 shows the absorption correction factor as a function of redshift with mean value of $F_{\text{int}}/F_{\text{obs}} = 1.05$. We denote an observed 2-10 keV flux as F_{obs} and an absorption corrected 2-10 keV flux in the observed frame as F_{int} .

Finally, given the large redshift range covered by our sample (see Figure 1), it is necessary to apply k-corrections to compute the X-ray rest-frame luminosities of our $70\mu\text{m}/\text{X-ray}$ galaxy sample, which we apply after the absorption correction. We assume that the spectrum of our galaxies in X-ray follows a simple power-law with photon index $\Gamma = 1.7$, and derive the ratio between rest-frame and observe-frame flux integration, to compute the rest-frame flux. Although using different Γ values could affect the derived k-correction factor, such variation is not significant. We apply a correction based on $\Gamma = 1.7$ to our $70\mu\text{m}/\text{X-ray}$ galaxies disregarding them being from the Chandra or XMM catalog.

To ensure the intrinsic 2-10keV luminosity robustness, we only estimate the absorption correction for those samples that have detection both in soft and hard band. It is worth noting that galaxies only detected in hard X-ray band (i.e. HR = 1) can also indicate the presence of Compton-thick AGNs ($N_H \geq 1.5 \times 10^{24} \text{ cm}^{-2}$). Compton-thick AGNs are usually included in X-ray background synthesis model to interpret the intensity peak about 30 keV (Comastri 2004). We try to quantify the fraction of obscured AGN in our sample by binning hard X-ray luminosity in a range of $41 \leq \log L_X < 43$, $43 \leq \log L_X < 45$, and $45 \leq \log L_X$. For each of these hard X-ray luminosity bins, the fraction of obscured AGNs with $\log N_H \geq 22$ to all AGNs (in the same hard X-ray luminosity range) is $\sim 44\%$, 48% , and 29% , respectively. Ueda et al. (2003) presented the hard X-ray luminosity function and absorption function of AGN up to redshift = 3. In Figure 7 of their paper, the obscured AGN fraction is $58 \pm 1\%$, $50 \pm 3\%$, and $34 \pm 5\%$ with corresponding hard X-ray luminosity range of $41.5 \leq \log L_X < 43$, $43 \leq \log L_X < 44.5$, and $44.5 \leq \log L_X$. We compare the obscured AGN fraction of $70\mu\text{m}/\text{X-ray}$ galaxies with Ueda et al. (2003). The obscured AGN fraction of the higher X-ray luminosity (i.e. $43 \leq \log L_X < 45$ and $45 \leq \log L_X$) in our study is comparable to Ueda et al. (2003). On the contrary, our lower X-ray luminosity (i.e. $41 \leq \log L_X < 43$) range, probably miss around 20% of obscured AGN, implying that the sample with this range loses more obscured AGNs relative to our higher X-ray luminosity sample. However, more recent studies inferred a different trend in the obscured AGN fraction than Ueda et al. (2003), in particular with a non-negligible incompleteness detected for very high luminosities ($\log L_X \geq 45$ - Gilli et al. 2007; Merloni et al. 2014). Fortunately, 70% of our sample with intrinsic 2-10keV luminosity information, is in a range of $43 \leq \log L_X < 45$, where the obscured fraction is comparable with the literature (e.g. Ueda et al. 2003; Gilli et al. 2007; Merloni et al. 2014; Ueda et al. 2014).

⁴ <http://heasarc.gsfc.nasa.gov/Tools/w3pimms.html>

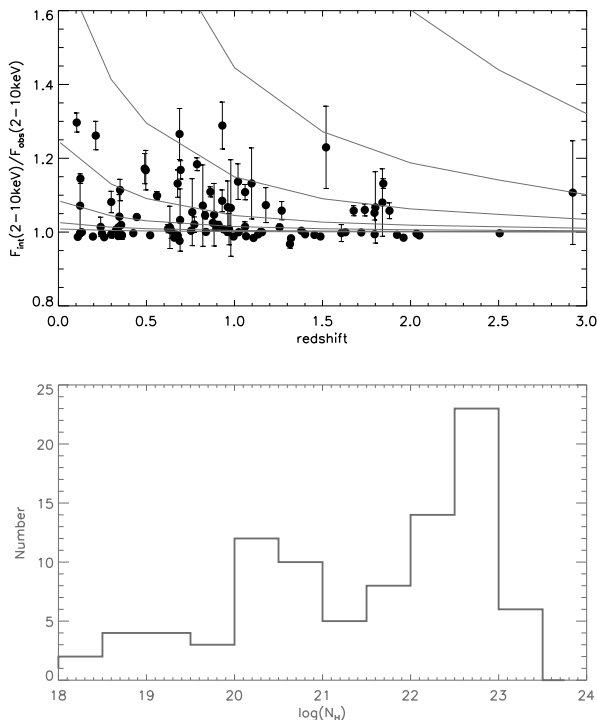


Figure 4. Top panel: The absorption correction factor $F_{int}(2-10\text{keV})/F_{obs}(2-10\text{keV})$ versus redshift. F_{obs} and F_{int} indicate an observed 2-10 keV flux and an absorption corrected 2-10 keV flux in observed frame. Error bar comes from 1σ dispersion of HR. The solid lines from bottom to top present different amount of $N_H = 1 \times 10^{21}$, 3×10^{21} , 1×10^{22} , 3×10^{22} , 1×10^{23} , 3×10^{23} , and $1 \times 10^{24} \text{ cm}^{-2}$, respectively. Absorption correction factors with < 1 are set to be 1. Bottom panel: The histogram of column density of $70\mu\text{m}/\text{X-ray}$ galaxies.

4 RESULTS

4.1 AGN versus star formation

Our sample is drawn from both $70\mu\text{m}$ and X-ray catalogs, the far-infrared detection indicates the presence of dust from associated star formation. In fact, the star formation may generate the X-ray emission by supernovae remnant and high mass X-ray binaries (HMXBs) instead of being generated by a single powerful AGN. Therefore, in this section, we try to use different methods to study the driving mechanism of $70\mu\text{m}/\text{X-ray}$ galaxies.

4.1.1 AGN criterion from colour-colour selection

The mid-infrared IRAC colour-colour selection described by Stern et al. (2005, hereafter S05) is widely accepted as a robust method to select AGN candidates. Such colour criteria are efficient to separate AGN candidates from star-forming galaxies due to the red $[3.6\mu\text{m}] - [4.5\mu\text{m}]$ colour inferred by the combination of the power-law continuum spectrum of the AGN and the relative weakness of the stellar bump feature at $1.6\mu\text{m}$ usually emitted by the host galaxy. Lacy et al. (2004) proposed another AGN diagnosis using a different IRAC colour-colour selection from S05. However, Choi et al. (2011) used complete AGN samples based on different selections (e.g. BPT diagram, $[\text{O III}]/\text{H}\beta$ ratio, high excitation line $[\text{Ne V}]$, and broad line region feature) and showed that the S05 colour-colour selection is more robust than Lacy et al. (2004).

In Figure 5 we show the IRAC $[3.6\mu\text{m}]-[4.5\mu\text{m}]$ vs. $[5.8\mu\text{m}]-[8.0\mu\text{m}]$ colour-colour diagram of our $70\mu\text{m}/\text{X-ray}$ galaxies. The deep pink line indicates the AGN dominating region defined by S05. Using these criteria, we separate AGNs from our star-forming galaxies, LIRGs, and ULIRGs. Their estimated AGN fractions are 20% (4 out of 20; blue stars), 48% (29 out of 60; green square), and 92% (57 out of 62; red cross), respectively. There are 63% (90 out of 142) of $70\mu\text{m}/\text{X-ray}$ galaxies classified as AGN from the S05 selection criteria. We observe that ULIRGs are overlapping more with AGN region in the diagram than the locus of star-forming galaxies; this result is consistent with literatures that demonstrate an increasing AGN fraction with increasing infrared luminosity (Franceschini et al. 2003; Lee et al. 2010; Wang et al. 2010).

Our sample spans a wide range of redshifts which may influence the observed colour-colour properties due to k-correction effect. To better quantify this redshift effect, we place the SED of templates in different redshifts and simulate the colour changes in Figure 5. Since 44% of our $70\mu\text{m}/\text{X-ray}$ galaxies (62 out of 142) are classified as ULIRGs, we used the SEDs of the ULIRG Mrk231, which has a strong AGN contribution in the mid-infrared band, and of Arp220, which has intense starburst activity, and shift them to the redshift range of $0 < z < 3$ (the ULIRGs in our sample span the redshift range of $z = 0.5$ to 3), then plot the colour changes. Based on its IR properties, Arp220 is considered as the prototypical ULIRG powered by star formation. Despite the detection of high ionization Fe K lines in its X-ray spectrum preventing us from completely ruling out the possibility of a low luminosity or Compton-thick AGN (Iwasawa et al. 2005), we still assume, as is commonly done in the literature, that Arp220 represents a star-formation dominated ULIRG. On the other hand, in the ULIRG Mrk231, the mid-infrared continuum can be well fitted by a power-law spectrum (Weedman et al. 2005) and the hard X-ray emission is dominated by an unresolved nuclear point source (Gallagher et al. 2002). It is unambiguously accepted that an AGN hosts in the centre. We use Mrk231 to represent an AGN-dominated ULIRG. In Figure 5, the Mrk231 colours remain in the S05 AGN region at any redshift because of its featureless power-law SED in mid-IR. In contrast, the Arp220 colours may satisfy the S05 AGN criteria in some redshift ranges because of the $3.3\mu\text{m}$, $6.2\mu\text{m}$, and $7.7\mu\text{m}$ PAH emission features entering into the IRAC photometry bands and confusing the AGN diagnosis. The S05 criteria are, therefore, not extremely robust against Arp220-like star formation dominating ULIRG.

However, 56% of $70\mu\text{m}/\text{X-ray}$ galaxies (80 out of 142) are not classified as ULIRGs, their L_{IR} cannot compete with Mrk231 and Arp220. Therefore, we place the SED of starburst galaxy M82 and main-sequence Sc-type spiral galaxy in the redshift range of $0 < z < 1$ (LIRGs and star-forming galaxies are below $z = 1$ in our sample) and simulate the colour changes. Figure 5 shows that in most redshift intervals, both M82 and Sc-type spiral galaxy are almost in the outside of the AGN boundaries. All SED templates used above come from the SWIRE galaxy library, and are a combination of models, photometric data, and observed IR spectra (Polletta et al. 2007, and references therein).

4.1.2 L_X vs. L_{IR} relation

The relation between hard X-ray luminosity and total infrared luminosity provides us with another method to determine whether star formation from host galaxy or AGN predominates the overall SED. While colour-colour selection can be altered by the presence of specific lines (Donley et al. 2008), total infrared luminosity is more ro-

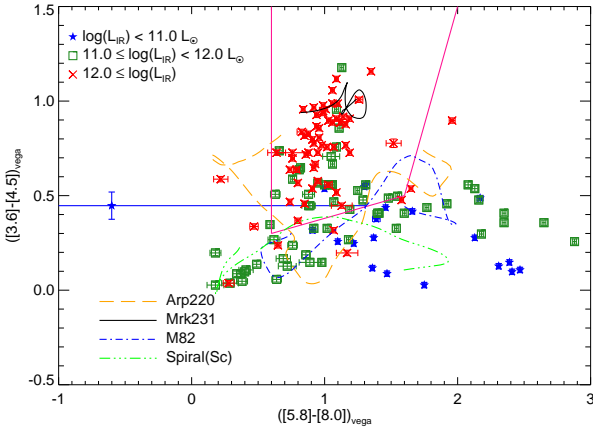


Figure 5. $[3.6]-[4.5]$ versus $[5.8]-[8.0]$ colour-colour diagram of $70\mu\text{m}/\text{X}$ -ray galaxies. The different L_{IR} -selected galaxy samples follow the description in Figure 1, with blue stars, green squares and red crosses indicating star-forming galaxies, LIRGs and ULIRGs, respectively. The pink solid line represents the boundaries of the AGN region defined by Stern et al. (2005). Orange dash line and black solid line represent the evolution with redshift from $z = 0$ to 3 of the colours of star-forming dominated ULIRG Arp220 and AGN-dominated ULIRG Mrk231, respectively. Blue dash-dot line and green dash-triple-dot line represent the evolution with redshift from $z = 0$ to 1 of the colours of starburst galaxy M82 and Sc-type spiral galaxy templates, respectively.

bust because it is derived from 8-1000 μm continuum (Smail et al. 2011).

In Figure 6 we display the absorption-corrected rest-frame hard X-ray (2 – 10keV) luminosity against k-corrected total (8 – 1000 μm) infrared luminosity for our $70\mu\text{m}/\text{X}$ -ray galaxies, which we divide into three subsamples according to their L_{IR} luminosity: star-forming galaxies, LIRGs, and ULIRGs (same symbols as in Figure 5). N_{H} absorption correction and k-correction have been applied to the hard X-ray luminosity for those 96 sources with HR measurement (please see Section 3.3 for details). For the remaining 46 sources without HR measurement, even if we have redshift information to perform a k-correction of X-ray luminosity, the lack of HR measurement prevents us from performing an N_{H} absorption correction, and therefore they are not included in Figure 6. The X-ray luminosity versus infrared luminosity plot shows a tight Spearman’s rank correlation coefficient, $\rho \sim 0.88$. (Note that Spearman’s $\rho = 1$ corresponds to two variables being monotonically related.) However, this strong correlation may be a manifestation of an observational bias. In order to understand this tight correlation, and whether it comes from the observational bias, we need to estimate the upper and lower limits in the L_{X} vs. L_{IR} plot. For the total infrared luminosity, we slice the whole $70\mu\text{m}$ catalog (Kartaltepe et al. 2010) into several redshift bins from $z = 0.033$ to $z = 3$, and identify the maximum and minimum total infrared luminosity. For the hard X-ray luminosity, we simulate the lower X-ray luminosity in the same redshift bins using the Chandra flux limits and measure the upper X-ray luminosity directly from the XMM catalog. The results are displayed as grey regions in Figure 6. These observational limits and their evolution with redshift indeed explain the tight correlation between the infrared and X-ray luminosities.

By studying X-ray properties of star-forming galaxies, Ranalli et al. (2003) demonstrated that the hard X-ray luminosity is also proportional to the star formation rate (SFR). This rela-

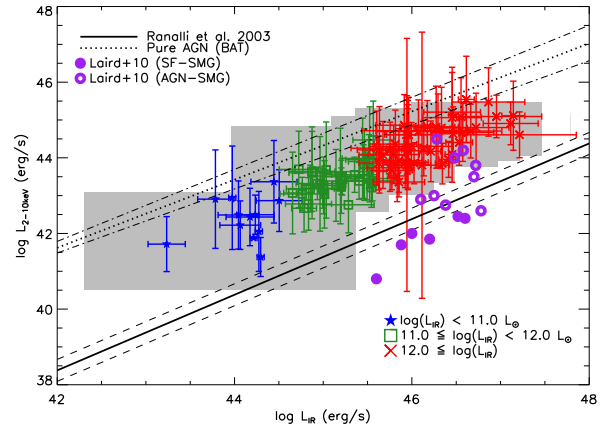


Figure 6. Absorption-corrected rest-frame 2-10keV luminosity versus total infrared luminosity of $70\mu\text{m}/\text{X}$ -ray galaxies. Symbols are the same as in Figure 5. The X-ray luminosity error bars are derived from the estimated flux errors, while the total infrared luminosity error bars are the 1σ uncertainty based on the result of Kartaltepe et al. (2010) template fit. Grey regions represent the areas covered by maximum and minimum luminosities in different redshifts bins drawn from the full X-ray selected and full $70\mu\text{m}$ selected samples. These observational limitations induce the apparent strong correlation between L_{X} and L_{IR} observed in COSMOS field. Black dot line and black solid line represent the L_{X} vs L_{IR} relations for pure AGNs (Mullaney et al. 2011) and star-forming galaxies (Ranalli et al. 2003), respectively. Dash-dot line and dash line represent 1σ dispersion of the L_{X} vs L_{IR} relations for pure AGNs and star-forming galaxies. Laird et al. (2010) separated the star forming submillimeter galaxies (SF-SMGs) and the AGN-hosted submillimeter galaxies (AGN-SMGs) from X-ray spectrum fitting. Fill and open circles represent SF-SMGs and AGN-SMGs, respectively.

tion between L_{X} and L_{IR} is represented by the black solid line in Figure 6. In fact, the most important contributors of X-ray emission in such galaxies are the high mass X-ray binaries (HMXBs). Franceschini et al. (2003) explored the X-ray properties of a sample of ULIRGs and most of them do not exhibit AGN signature. The conclusion of their work is that the X-ray luminosity and spectral shape of some ULIRGs are dominated by hot thermal plasma and X-ray binaries originating in recent starburst region.

On the other hand, because of the presence of the parsec-scale dust “torus” surrounding the accretion disk of the central SMBHs, AGNs emit light in the infrared wavelength (Gandhi et al. 2009). Indeed, the ultraviolet and optical light emitted by the central accretion disk is absorbed by the dust and re-emitted in infrared. Gandhi et al. (2009) observed the core of nearby AGNs with unprecedentedly high spatial resolutions in both mid-IR and X-ray wavelength, demonstrating a strong correlation between 12.3 μm and hard X-ray luminosities. Although, the rest-frame at 12.3 μm could be influenced by the PAH emission feature at 11.3 μm , the dispersion of $L_{\text{X}}/L_{12.3\mu\text{m}}$ is quite small which may be due to statistical uncertainty rather than physical reasons (Lutz et al. 2004; Gandhi et al. 2009). Based on the intrinsic AGN/quasar IR SED from Netzer et al. (2007), Mullaney et al. (2011) established an empirical relation between the 12.3 μm luminosity and the AGN infrared luminosity (see Figure 11 of their paper). By combining with the relation between 12.3 μm and hard X-ray luminosities established by Gandhi et al. (2009), Mullaney et al. (2011) derived an unbiased L_{X} vs. L_{IR} relation for AGNs (see equation (4) of their paper), free of any contamination from the host galaxy. This “pure”

AGN L_X vs. L_{IR} relation is represented by the dotted line in Figure 6. This relation is confirmed observationally by combining the swift-BAT X-ray selected AGN population (Tueller et al. 2010), together with IRAS infrared measurements (BAT/IRAS AGN). The strong $60\mu\text{m}$ luminosity of this population is more likely powered by the AGN rather than star formation activity from the host galaxy, as demonstrated by the linearly increasing correlation between L_{IR} and L_X (Mullaney et al. 2012). In addition the hard energy band of swift-BAT observation (14-195 keV) enables a selection of galaxies unbiased against obscuration.

As shown in Figure 6, the L_X and L_{IR} distribution of our $70\mu\text{m}/\text{X-ray}$ galaxies deviates from these established "pure" AGN and "pure" star forming relation by 0.5 – 1 dex and 1 – 2 dex, respectively. Ignoring the pure-AGN and pure-SF relations are affected by any observational bias, our sample indicates a higher AGN activity relative to star formation. An important note of caution is that this result is strongly dependent of observational limits, as shown by the grey region of Figure 6. Because shallow X-ray observations in COSMOS are limited in the detection of "pure" star forming galaxies, especially at high redshift, our sample is biased toward most sources with higher X-ray emission, likely to host an AGN. On the other hand, for a given L_X , a higher L_{IR} may indicate a contamination from star formation in the host galaxy, shifting our sample away from a pure AGN relation in the L_X vs L_{IR} diagram.

It is also interesting to compare the properties of our sample with a sample of Submillimeter galaxies (SMGs); a population of objects selected according to their detection in submillimeter wavelengths. This population is dominated by strongly star-forming cold-dust enshrouded galaxies at high redshift (e.g. Chapman et al. 2005). The concomitance in redshifts and total infrared luminosities with ULIRGs may indicate that SMGs are an early stage of evolution of the merger scenario (Greve et al. 2005; Biggs & Ivison 2008; Engel et al. 2010). Ultra-deep X-ray observations of those distant star-forming galaxies indicate that 20-30% of SMGs host an AGN (Alexander et al. 2005). Laird et al. (2010) have studied the X-ray spectral properties of SMGs and classified them as AGN or starburst. These objects are represented in Figure 6 with open and closed purple circles, respectively. Our $70\mu\text{m}/\text{X-ray}$ galaxies appear to share similar L_X vs. L_{IR} relation as the AGN-hosted SMGs.

In summary, all indicators in the L_X vs. L_{IR} distribution of our $70\mu\text{m}/\text{X-ray}$ galaxies suggest that there is a significant contribution from AGN activity in the X-ray band relative to pure star formation.

4.2 Hardness ratio of $70\mu\text{m}/\text{X-ray}$ galaxies

To explain the diversity of AGNs (e.g., narrow-lines vs. broad-lines), an unified model based on the variation of obscuration due to the orientation of the dust torus surrounding the SMBH accretion disk, has been proposed. In such model, the presence of an edge-on dust torus not only blocks the broad-line emissions, but also increases the absorption in soft X-ray because of the higher hydrogen column density (Antonucci 1993).

In parallel, galaxy mergers can accumulate large amount of neutral hydrogen and also trigger star formation (e.g., Esquej et al. 2012). Using the Extended Chandra Deep Field-South (ECDF-S) dataset, Treister et al. (2009) showed that AGNs residing in star-forming galaxy display large absorption in soft X-ray emission, indicating a large amount of neutral hydrogen existing along the direction of line-of-sight.

Our aim through this work is to investigate whether there is a direct connection between the obscuration properties of the AGN

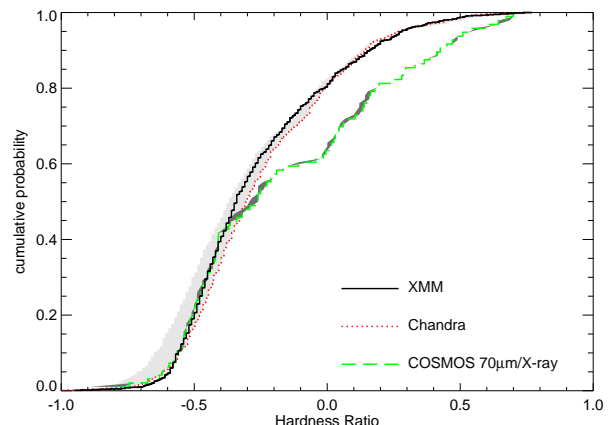


Figure 7. Kolmogorov-Smirnov test: the hardness ratio cumulative probability distribution of XMM, Chandra, and $70\mu\text{m}/\text{X-ray}$ selected samples are represented in black solid, red dotted, and green dash colour lines, respectively. The sample number of XMM, Chandra, and $70\mu\text{m}/\text{X-ray}$ selected samples are 1001, 920, and 96. The light grey and dark grey regions represent the $1-\sigma$ uncertainties in HR conversion equation of Chandra and $70\mu\text{m}/\text{X-ray}$ sample. The mean values (1σ) of hardness ratio of XMM selected sample, Chandra selected sample, and $70\mu\text{m}/\text{X-ray}$ sample are $-0.26 (\pm 0.28)$, $-0.28 (\pm 0.29)$, and $-0.16 (\pm 0.39)$, respectively. Distribution of XMM and Chandra indicate these samples are drawn from the same population. However, the distribution of $70\mu\text{m}/\text{X-ray}$ sample and X-ray selected samples seem not to be drawn from the same population. The distributions indicate an excess of $\text{HR} \geq -0.3$, revealing that the cold dust from the host galaxy may be responsible for additional obscuration.

and those of the host galaxy. As absorption affects the soft X-ray emissions more than the hard X-ray emissions, the HR is a good tracer of obscuration, with higher value of HR corresponding to larger absorption. We apply Kolmogorov-Smirnov (K-S) test on two datasets, X-ray selected galaxies and $70\mu\text{m}/\text{X-ray}$ galaxies, to address their likelihood to be drawn from the same sample (i.e. our null hypothesis) (*Numerical Recipes*, Press et al. 1992).

As an initial test, we apply the K-S test on the HR measurements of both XMM and Chandra X-ray selected sources to test the robustness of our conversion between the two systems (for details, see section 3.3). The results of our K-S test for these populations are shown in Figure 7, with the HR cumulative probability distribution of XMM selected sample in black and Chandra selected sample in red, and the K-S parameters are summarized in Table 3. The probability of K-S test for XMM and Chandra selected sample to be drawn from the same population is only 3%, which is not significant enough to reject the null hypothesis (our threshold to reject the null hypothesis is 99%; in other words, a probability smaller than 0.01 rejects the null hypothesis).

The size of the XMM and Chandra selected samples is 1001 and 920 sources, respectively, which is larger than the 96 sources included in our $70\mu\text{m}/\text{X-ray}$ galaxy sample. In order to better understand how sample size impacts the results of our K-S test, we proceed in a simple random sampling method. We randomly select 96 sources out of the XMM (Chandra) selected sample and run a K-S test between this subsample and the Chandra (XMM) selected sample. This procedure has been repeated for 1000 times to estimate probability mean and standard deviation. Following this procedure, we estimate that the probability of K-S test for XMM and Chandra selected sample to be drawn from the same population can be as high as $\sim 40\%$ when including the sample size errors; these

results are summarized in rows 2 and 3 of Table 3. Although two X-ray facilities have different sky coverage and depth, both XMM and Chandra HR distribution are roughly identical.

Thereafter, we apply the K-S test on the $70\mu\text{m}/\text{X-ray}$ and XMM selected samples. This time, the null hypothesis is rejected at a significance of 99% confidence level, implying that $70\mu\text{m}/\text{X-ray}$ galaxies and XMM galaxies are drawn from different populations. The K-S test on $70\mu\text{m}/\text{X-ray}$ and Chandra selected samples also rejects the hypothesis. The probability for both samples to be drawn from the same population is 0.3% for XMM & $70\mu\text{m}/\text{X-ray}$ sample, and 0.2% for Chandra & $70\mu\text{m}/\text{X-ray}$ sample. Figure 7 displays the cumulative probability distribution of HR from XMM (black solid line), Chandra (red dotted line), and $70\mu\text{m}/\text{X-ray}$ (green dash line) selected samples. The light grey and grey regions represent the effect on the cumulative distribution of HR of a $1-\sigma$ uncertainty implied by our HR conversion equation on the Chandra and $70\mu\text{m}/\text{X-ray}$ samples (as discussed in section 3.3). Even when the HR conversion equation applied on the Chandra sample varies within a $1-\sigma$ uncertainty (see Equation (2)), the cumulative distribution of both XMM and Chandra HR ratios are similar and the cumulative distribution of $70\mu\text{m}/\text{X-ray}$ HR is consistent with this sample not being drawn from the same population than XMM/Chandra purely X-ray selected samples. The K-S parameters resulting from the three tests are summarized in Table 3. It is useful to note that in above analysis the $70\mu\text{m}/\text{X-ray}$ detected sources are included in the XMM and Chandra selected samples. But even if we exclude the $70\mu\text{m}/\text{X-ray}$ detected sources from the XMM and Chandra selected samples, the main results of the K-S tests do not change.

In fact, the cumulative probability distribution below $\text{HR} \sim -0.3$ is identical for the $70\mu\text{m}/\text{X-ray}$ galaxies and pure X-ray selected samples (either from XMM or Chandra observation), indicating that the fraction of unobscured AGNs is uniform over the full sample. On the opposite, the obvious diversity of cumulative probability distribution appears above $\text{HR} \sim -0.3$: there are 80% of AGNs with $\text{HR} \leq 0$ in the pure X-ray selected sample, while there are only 60% of AGNs in the $70\mu\text{m}/\text{X-ray}$ galaxy sample. According to column densities we derived from the HR measurements, the mean value of N_H for the overall $70\mu\text{m}/\text{X-ray}$ galaxy sample is $\sim 10^{22} \text{ cm}^{-2}$, which is consistent with a mildly absorbed AGN population. However, the $70\mu\text{m}/\text{X-ray}$ sample contains 21 galaxies detected only in the hard X-ray which are potential Compton-thick AGN (21/142; 15%). These are obviously not included in our K-S tests because of lack of HR measurements, and they can potentially increase the difference between $70\mu\text{m}/\text{X-ray}$ galaxies and pure X-ray selected samples. It may be useful to mention that, for XMM and Chandra selected sample, the fraction of the sources that only have hard X-ray detection is 12% (213/1797) and 15% (257/1761), respectively. These fractions are consistent with those found for the $70\mu\text{m}/\text{X-ray}$ galaxy sample. In order to estimate the column density for 21 hard X-ray detected $70\mu\text{m}/\text{X-ray}$ galaxies, given a known redshift, we can constrain their soft X-ray count rate from the flux limit of the observations and then calculate the lower limit of HR. Following the same procedure we used for $70\mu\text{m}/\text{X-ray}$ galaxies with HRs measurements (see Section 3.3), we obtain a mean value of column density of at least $\sim 10^{23} \text{ cm}^{-2}$ for those 21 hard X-ray detected $70\mu\text{m}/\text{X-ray}$ galaxies. Among these 21 hard X-ray detected $70\mu\text{m}/\text{X-ray}$ galaxies, one object ($70\mu\text{m}$ ID = 1539) has high probability to be a Compton-thick AGN with the lower limit of $\text{HR} \sim 0.921$, corresponding to $N_H \sim 1.45 \times 10^{24} \text{ cm}^{-2}$. With its photometric redshift ($z=2.36$), the derived total infrared luminosity may exceed $10^{13} L_\odot$, putting this object in the 'hyper

ULIRG' category. The exclusion of such objects from our analyses only reinforce the conclusions of our K-S tests that $70\mu\text{m}/\text{X-ray}$ galaxies are not from the same population as the full X-ray selected samples. On the other hand, there are 24 soft X-ray detected $70\mu\text{m}/\text{X-ray}$ galaxies not included in our K-S tests because of lack of HR measurements, which can potentially influence the results. We adopt the hard X-ray count rate from flux limit of the observation and derive the upper limit of hardness ratio. A corresponding mean value of column density for soft X-ray detected $70\mu\text{m}/\text{X-ray}$ galaxies is lower than $\sim 10^{20} \text{ cm}^{-2}$. It is important to note that the main results of K-S tests presented in this section does not change qualitatively if we included the soft X-ray detected $70\mu\text{m}/\text{X-ray}$ galaxies.

Our tests lead to the conclusion that the $70\mu\text{m}/\text{X-ray}$ galaxies include more obscured AGNs than pure X-ray selected samples. This result implies an additional process responsible for an increased N_H in the line-of-sight of AGNs hosted by dust-enshrouded galaxies; process not accounted for in the conventional AGN unified model scheme. We speculate that the excess of obscuration is not only attributed to absorption on the line-of-sight by continuum or clumpy dust torus around the SMBH, but also is associated with an additional more diffused dust component generated by strong star formation in the host galaxy. In this case, the starburst could be the consequence of an event involving the whole system (e.g. merger) or generated by the circumnuclear region (e.g. bar). Kartaltepe et al. (2010b) have identified that the merger fraction (either major mergers or minor mergers) and AGN fraction increase systematically with increasing infrared luminosity (especially ULIRGs) in $70\mu\text{m}$ -selected galaxies. The excess of obscured AGNs in our study could support the merger scenario; an intense starburst triggered by mergers produces large amount of dust and gas, which tends to hide the central AGN.

4.3 Far-infrared colour of host galaxy

According to the predictions from the merger scenario, galaxy interaction triggers massive star formation, while at the same time, it disturbs the gas distribution, funneling it toward the central black hole, feeding the accretion disk, and therefore, generating a phase of nuclear activity (Imanishi et al. 2010). If the center of the galaxy harbors an AGN, dust in the host galaxy could be influenced by the radiations produced by the nucleus.

In order to determine the temperature of cold dust component, ideally one would like to measure fluxes in the Rayleigh-Jeans tail of the blackbody, at longer wavelength such as $160\mu\text{m}$. Far-infrared photometry is an indicator of the dust properties of the galaxy. In our $70\mu\text{m}/\text{X-ray}$ galaxies sample, there are 52 galaxies that have $160\mu\text{m}$ detection (52 out of 142; 37%). This fraction is comparable to that of the $160\mu\text{m}$ -detected $70\mu\text{m}$ sources (463 out of 1503; 31%) with or without X-ray detection. Measuring colours at longer wavelength is a method to estimate the cold dust temperature (Casey 2012). To explore whether the cold dust temperatures of $70\mu\text{m}/\text{X-ray}$ and $70\mu\text{m}$ galaxies differ, we use the observed frame colour in $\log(F_{70\mu\text{m}}/F_{160\mu\text{m}})$ as a proxy of the SED in far-infrared. A caveat of this method is that the rest-frame far-infrared photometry corresponding to the observed photometry shifts toward shorter wavelength as the redshifts of the galaxies increase, limiting our ability to reliably measure the cold dust temperature at higher redshifts.

The top panel of Figure 8 plots the $\log(F_{70\mu\text{m}}/F_{160\mu\text{m}})$ colour distribution of $70\mu\text{m}$ galaxies (black colour) and $70\mu\text{m}/\text{X-ray}$ galaxies (red colour) as a function of redshift. $70\mu\text{m}$ galaxies

Table 3. Results of the K-S test on the hardness ratio between different catalogs. The randomly selected subsample are marked with an asterisk. Their mean value and standard deviation are computed with 1000 time random selection.

Sample 1	Number (sample 1)	Sample 2	Number (sample 2)	D_{\max}	Significant	Hypothesis (p=0.01)
XMM	1001	Chandra	920	0.0664	0.0279	Not Reject
XMM	1001	Chandra (Subsample)*	96	0.100 ± 0.026	0.397 ± 0.261	Not Reject
Chandra	920	XMM (Subsample)*	96	0.0967 ± 0.022	0.423 ± 0.238	Not Reject
XMM	1001	70 μm /X-ray	96	0.1920	0.0026	Reject
Chandra	920	70 μm /X-ray	96	0.1981	0.0018	Reject

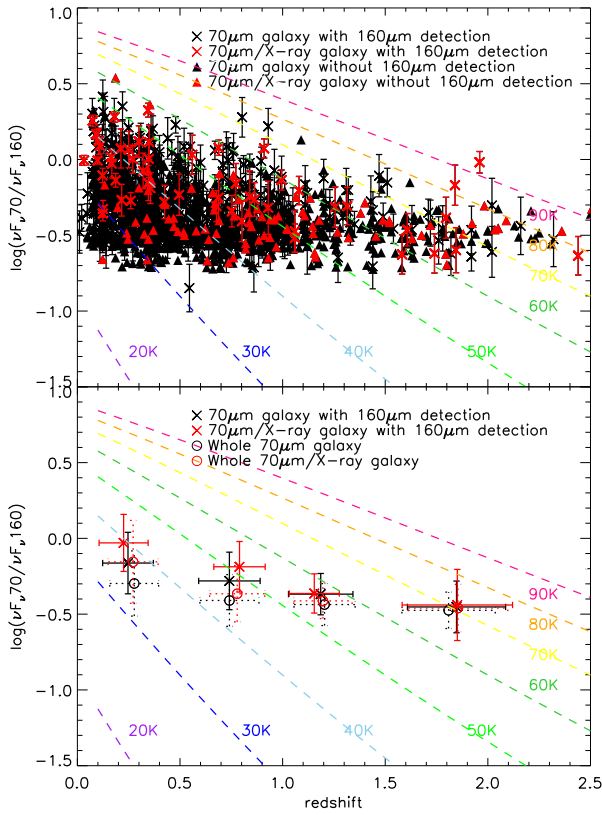


Figure 8. Top panel: observed frame $\log(F_{70\mu\text{m}}/F_{160\mu\text{m}})$ as a function of redshift; black and red symbols refer to all 70 μm galaxies and 70 μm /X-ray galaxies, respectively. 70 μm galaxies with and without 160 μm detection are labeled as crosses and triangles, respectively. Dash lines in different colours show the simulated $\log(F_{70\mu\text{m}}/F_{160\mu\text{m}})$ as a function of redshift in different temperatures, derived from modified blackbody model with a given temperature. Bottom panel: Average $\log(F_{70\mu\text{m}}/F_{160\mu\text{m}})$ in observed frame versus redshift. Labeled colours and lines are same to top panel. Crosses represent the mean $\log(F_{70\mu\text{m}}/F_{160\mu\text{m}})$ of 70 μm galaxies (or 70 μm /X-ray galaxies) with 160 μm detection. Open circles refer to the mean $\log(F_{70\mu\text{m}}/F_{160\mu\text{m}})$ of whole 70 μm galaxies (or whole 70 μm /X-ray galaxies), including those which only have lower limits. The error bars are the standard deviation of colour and redshift.

with 160 μm detection are labeled as crosses, while 70 μm galaxies without 160 detection are labeled as triangles. For those 70 μm galaxies without 160 μm detection, we set 50mJy as limiting flux density to measure lower limits of $\log(F_{70\mu\text{m}}/F_{160\mu\text{m}})$. A limit of 50mJy results from iterating between the source extraction at dif-

ferent limiting flux densities and the confusion noise measurements until they converge to a ratio of 5; details are described in Sec. 5.2 of Frayer et al. (2009). Dash lines with varied colours represent the simulated $\log(F_{70\mu\text{m}}/F_{160\mu\text{m}})$ colours for different dust temperatures. When simulating the far-infrared colour, we only assume one cold dust temperature component. The synthetic MIPS photometry of 70 μm and 160 μm are obtained by performing the IDL routine, which assigns a temperature as an input blackbody spectrum to simulate photometric flux density (refer to Spitzer Data Analysis Cookbook⁵, Recipe. 9). We slightly adjust this blackbody model by adding an emissivity parameter β , represented as an modified blackbody model:

$$\nu F_{\nu, \text{model}} = \nu^{\beta} B_{\nu}(\nu, T) \quad (3)$$

with a fixed emissivity $\beta \sim 1.5$ (Clements et al. 2010). To understand the far-infrared colour evolving with redshift, we shift filters to rest-frame wavelengths and then measure the simulated $\log(F_{70\mu\text{m}}/F_{160\mu\text{m}})$ colour with a given redshift. We assign the temperature, ranging from 30K to 90K, typical dust temperatures for submillimeter galaxies (SMGs) and ULIRGs (Chapman et al. 2005; Kovács et al. 2006; Yang et al. 2007; Casey et al. 2009).

In the bottom panel of Figure 8, the mean $\log(F_{70\mu\text{m}}/F_{160\mu\text{m}})$ colour of our X-ray detected and not X-ray-detected 70 μm galaxies are represented by red and black colours, respectively. The error bars are estimated from the standard deviation of $\log(F_{70\mu\text{m}}/F_{160\mu\text{m}})$ and redshift. Crosses and open circles represent the mean $\log(F_{70\mu\text{m}}/F_{160\mu\text{m}})$ colour of 70 μm galaxies with and without 160 μm detection, respectively. For the sources without a 160 μm limiting flux density as previously stated, and measure the lower limits of $\log(F_{70\mu\text{m}}/F_{160\mu\text{m}})$. Given the large uncertainties, the average far-infrared colours for the 70 μm galaxies and the 70 μm /X-ray galaxies are similar in the same redshift interval. We do not see any significant difference in far-infrared colour between these two samples.

5 DISSUSSION

5.1 AGN influence on the host galaxy dust temperature?

Our analysis in section 4.3 shows that there is no difference in the far-infrared colour (i.e. $\log(F_{70\mu\text{m}}/F_{160\mu\text{m}})$) of 70 μm and 70 μm /X-ray galaxy samples at all redshift. This result is in agreement with Elbaz et al. (2010), who derived an accurate estimation

⁵ <http://irsa.ipac.caltech.edu/data/SPITZER/docs/dataanalysisstools/cookbook/>

of the cold dust temperature of the host galaxy by using the Herschel photometry in the $250\mu\text{m}$, $350\mu\text{m}$, and $500\mu\text{m}$ bands on the Rayleigh-Jeans portion of the spectra. Their precise measurements show that, given the large error bars, the cold dust temperatures of galaxies with and without AGN are consistent. In fact that there is no difference in far-infrared colours can be attributed to the different spatial scales between AGN and star formation: the cold dust is distributed across the several kpc scale of the galaxy and the energy released by the AGN may be insufficient to heat the dust at such scale. This implies that the mechanism of FIR emission in galaxies is mainly due to star formation disregarding the presence of an AGN.

Using infrared colour $\log(F_{24\mu\text{m}}/F_{70\mu\text{m}})$ to sample the blackbody temperature profile, Rafferty et al. (2011) concluded that galaxies hosting an AGN present a warm dust temperature. We reproduce their analysis for our sample, as shown in Figure 9. The $70\mu\text{m}$ galaxies have a median colour index of $\log(F_{24\mu\text{m}}/F_{70\mu\text{m}}) \sim -1.27 \pm 0.28$, while the $70\mu\text{m}/\text{X-ray}$ galaxies have $\log(F_{24\mu\text{m}}/F_{70\mu\text{m}}) \sim -0.99 \pm 0.30$. We apply the K-S test for these two samples; the probability to be drawn from the same population is $\ll 0.01\%$, indicating the difference between two $\log(F_{24\mu\text{m}}/F_{70\mu\text{m}})$ colour distributions in Figure 9 is statistically significant. The $70\mu\text{m}/\text{X-ray}$ galaxies present a higher colour index on average than overall $70\mu\text{m}$ galaxies at all redshifts, suggesting the presence of a warmer dust component, a similar conclusion to Rafferty et al. (2011). In fact, the $24\mu\text{m}$ band is sensitive to warm dust around AGN, explaining the discrepancies in $\log(F_{24\mu\text{m}}/F_{70\mu\text{m}})$ colour between X-ray detected and undetected $70\mu\text{m}$ galaxies. It is noted that $\log(F_{24\mu\text{m}}/F_{70\mu\text{m}})$ and $\log(F_{70\mu\text{m}}/F_{160\mu\text{m}})$ trace different dust temperature components.

To explain the difference in colour index, we look at the evolution of the $\log(F_{24\mu\text{m}}/F_{70\mu\text{m}})$ colour as a function of the redshift for four templates, the star-forming ULIRG Arp220, the AGN ULIRG Mrk231, the starburst galaxy M82, and the Sc-type spiral galaxy. Templates were described in Section 4.1.1. In the case of Arp220, the rest-frame $9.7\mu\text{m}$ absorption feature is shifted into the $24\mu\text{m}$ band at redshift $z \sim 1.5$ causing an apparent lower value of the colour index. Similarly, at $z > 2$ the 7.7 and $8.2\mu\text{m}$ PAH emission features enter the $24\mu\text{m}$ band, raising the $F_{24\mu\text{m}}/F_{70\mu\text{m}}$ flux ratio. In the case of Mrk231, the AGN driven power-law continuum produces colour index with little variation for various redshifts. In the case of M82, its $\log(F_{24\mu\text{m}}/F_{70\mu\text{m}})$ colour is similar to Mrk231 but with lower L_{IR} . However, M82 can only explain the $\log(F_{24\mu\text{m}}/F_{70\mu\text{m}})$ colour of star forming galaxies at $z < 0.5$, as such objects are rare at high redshift in our sample. In the case of the main-sequence Sc-type spiral galaxy, because of the weakest infrared luminosity, the $\log(F_{24\mu\text{m}}/F_{70\mu\text{m}})$ colour is bluer than the other three templates.

In Section 4.1.2, we show the possibility of higher AGN activity relative to star formation in $70\mu\text{m}/\text{X-ray}$ galaxies. This result is supported by the higher mean value of $\log(F_{24\mu\text{m}}/F_{70\mu\text{m}})$ in Figure 9, in which the $24\mu\text{m}$ of $70\mu\text{m}/\text{X-ray}$ galaxies are powered by AGN. The $70\mu\text{m}/\text{X-ray}$ galaxies follow the similar $\log(F_{24\mu\text{m}}/F_{70\mu\text{m}})$ colours of the X-ray luminous galaxy, Mrk 231, across the redshift range $0 < z < 3$; while for most $70\mu\text{m}$ galaxies, they follow the values between Arp220-like and M82-like galaxies.

5.2 AGN obscuration from starburst?

According to the major merger scenario of galaxy evolution, developed to interpret a potential ULIRG-QSO connection, galaxies un-

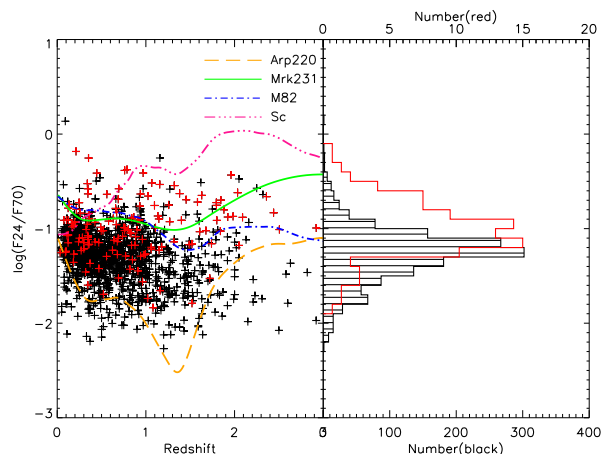


Figure 9. Distribution of $\log(F_{24\mu\text{m}}/F_{70\mu\text{m}})$ colour index for $70\mu\text{m}$ selected sample and $70\mu\text{m}/\text{X-ray}$ sample. *Left panel* : Distribution of the colour against redshift for the $70\mu\text{m}$ galaxies (black crosses) and the $70\mu\text{m}/\text{X-ray}$ sample (red crosses). The green solid line, orange dash line, blue dash dot line, and pink dash dot dot dot line indicate the evolution of Mrk231, Arp220, M82, and normal spiral galaxy flux ratio as a function of redshift by using the templates from Polletta et al. (2007). *Right panel* : Histogram of the colour index for $70\mu\text{m}$ -selected galaxies is black and $70\mu\text{m}/\text{X-ray}$ is red. The red histogram has been normalized to the peak of black sample for a better illustration (bottom and top axis represent the number of $70\mu\text{m}$ -selected galaxies and $70\mu\text{m}/\text{X-ray}$, respectively). The $70\mu\text{m}$ galaxies have a median colour index of $\log(F_{24\mu\text{m}}/F_{70\mu\text{m}}) \sim -1.27 \pm 0.28$, while the $70\mu\text{m}/\text{X-ray}$ galaxies have $\log(F_{24\mu\text{m}}/F_{70\mu\text{m}}) \sim -0.99 \pm 0.3$. Both satisfy the local cold dust definition of $\log(F_{24\mu\text{m}}/F_{70\mu\text{m}}) \leq -0.7$ (de Grijp et al. 1985; Sanders et al. 1988b).

dergo an obscuration phase after the merger occurred due to an increase in star formation and dust production. This obscured phase is thought to be succeeded by a consecutive AGN phase during which feedback from the central SMBH repels the dust (Hopkins et al. 2008). As an illustration, the NGC 6240, low-ionization nuclear emission-line regions (LINER), is a well-studied ULIRG with high infrared luminosity, indicating a starburst activity that generates a large amount of dust and molecular gas (Iono et al. 2007). A detailed X-ray spectrum from BeppoSAX of NGC 6240 reveals a very strong absorption with $N_H \sim 2 \times 10^{24} \text{ cm}^{-2}$ (Vignati et al. 1999). Deep Chandra observations provide high spatial resolution X-ray map of NGC 6240 and reveal the presence of a double AGNs system hidden in the core of the galaxy (Komossa et al. 2003). These observations are consistent with the idea that galaxies were formed as a consequence of a merger.

To efficiently investigate the concomitant evolutionary stages of the AGN and star formation, our approach is to study the properties of galaxies detected in both infrared and X-ray. Rafferty et al. (2011) had taken a similar approach to ours, looking for the X-ray counterpart of $70\mu\text{m}$ -selected galaxies in the ECDF-S, CDF-S, and EGS fields. They performed both a X-ray spectrum and X-ray band ratio analysis, assuming a power-law spectrum, and derived neutral hydrogen column densities for their $70\mu\text{m}$ -selected X-ray and full X-ray selected AGN samples. The N_H from Rafferty et al. (2011) results ranged between 10^{20} and 10^{23} cm^{-2} , which is consistent with our mean value of $N_H \sim 10^{22} \text{ cm}^{-2}$. Both Rafferty et al. (2011) and our work have identified one possible Compton-thick AGN comparable to the X-ray properties of ULIRGs in the local universe. However, they did not identify any excess of neutral hy-

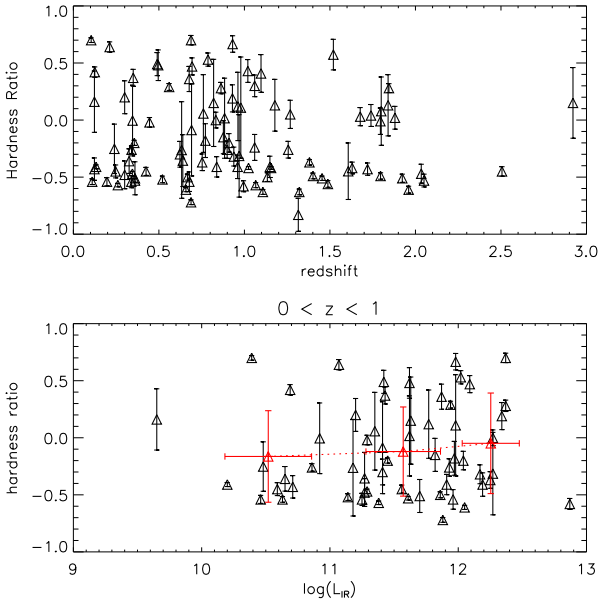


Figure 10. Top Panel: hardness ratio as a function of redshift, $70\mu\text{m}$ /X-ray galaxies are labeled as black triangles. Bottom panel: hardness ratio versus $\log(L_{IR})$ of $70\mu\text{m}$ /X-ray galaxies at the redshift range of $0 < z < 1$. Red triangles represent the mean hardness ratio of $70\mu\text{m}$ /X-ray galaxies in three different $\log(L_{IR})$ intervals. The x-axis and y-axis error bars are the $1-\sigma$ standard deviation of hardness ratio and $\log(L_{IR})$, respectively.

drogen in $70\mu\text{m}$ -selected X-ray sources compared to other X-ray selected AGNs (Figure 4 in Rafferty et al. (2011) paper), in contrast with our result. Their result implies that the obscured AGN population is not higher among the $70\mu\text{m}$ -selected X-ray sources, which contradicts the predictions of current AGN/starburst co-evolution models (Hopkins et al. 2008). The main reason why Rafferty et al. (2011) have a different result to us, is probably that there are more ($\sim 15\%$) $70\mu\text{m}$ /X-ray galaxies at $0 < z < 1$ in our sample. In this redshift range, we find a large obscured AGN population (i.e. more AGNs with higher HR values; see the top panel of Figure 10), which leads to the conclusion that $70\mu\text{m}$ /X-ray galaxies more often contain obscured AGNs. On the other hand, we lack $\sim 15\%$ $70\mu\text{m}$ /X-ray galaxies at the redshift $z > 2$. In Figure 10, the top panel shows the HR as a function of redshift, higher values of HR are concentrated in the lower redshift bins. In contrast, the HRs of the higher redshift galaxies are relatively low. This result is expected because the rest-frame bands shift to higher frequency at high redshift, and so the HR becomes less sensitive to absorption. The bottom panel of Figure 10 shows the HR versus $\log(L_{IR})$ at $0 < z < 1$. Given the large uncertainties, there is no apparent dependence between HR and $\log(L_{IR})$. The mean HR is constant across the full $\log(L_{IR})$ range.

Trichas et al. (2009) attempted a similar approach to our by studying the X-ray sources with $70\mu\text{m}$ counterparts in the redshift range $0.5 < z < 1.3$ from SWIRE survey. However, the K-S test resulted in a 3% probability of X-ray sources with $70\mu\text{m}$ detection to be drawn from a purely X-ray selected sample. In fact their low statistic probably did not enable them to draw any robust conclusion on whether $70\mu\text{m}$ detected X-ray galaxies were different from the global X-ray population. In contrast, we use the opposite selection method by selecting $70\mu\text{m}$ sources with X-ray counterparts and push to higher redshift ($z \sim 3$) taking advantage of the

COSMOS dataset. Owing to the twice times deeper $70\mu\text{m}$ observations in the COSMOS field we could identify a larger $70\mu\text{m}$ /X-ray galaxy sample (142 galaxies) which enables us to perform a proper statistical study. We, therefore, take a different approach by applying a K-S test on the distribution of hardness ratio to investigate if $70\mu\text{m}$ /X-ray galaxies and X-ray selected AGNs are drawn from the same sample (see section 4.2). Our K-S test concludes in less than 0.3% of probability for $70\mu\text{m}$ /X-ray galaxies to be drawn from a purely X-ray selected sample.

6 CONCLUSION

We have investigated the properties of 142 galaxies both detected in X-ray and $70\mu\text{m}$ in the COSMOS field. X-ray data are obtained from both XMM and Chandra point source catalogs, and $70\mu\text{m}$ photometry is drawn from Spitzer-MIPS $70\mu\text{m}$ point source catalog. We classify our sample into three distinct subsamples according to their respective total infrared luminosity (L_{IR}): star-forming galaxies ($L_{IR} < 10^{11} L_{\odot}$), luminous infrared galaxies (LIRGs, $10^{11} L_{\odot} \leq L_{IR} < 10^{12} L_{\odot}$), and ultra-luminous infrared galaxies (ULIRGs, $L_{IR} \geq 10^{12} L_{\odot}$), with median redshifts of $z \sim 0.168$, 0.518 and 1.268, respectively. The major conclusions of this study are as follows:

- (i) We apply two methods to determine the physical mechanism shaping the SED of our objects, star formation or AGN:
 - a) Using Spitzer-IRAC colours, we have shown that the majority (63%) of our sample are classified as AGN. The AGN fraction is seen to increase with increasing total infrared luminosity (L_{IR}).
 - b) Using the relation between absorption corrected rest-frame hard X-ray luminosity L_X (2-10keV) and total infrared luminosity L_{IR} (8-1000 μm), we find that $70\mu\text{m}$ /X-ray galaxies have higher AGN activity relative to star formation.
- (ii) Investigating the X-ray HR of our sample, we provide evidences for additional X-ray absorption in the $70\mu\text{m}$ /X-ray galaxies compared to typical X-ray selected AGN samples, in agreement with the predictions of current AGN/starburst co-evolution models (Hopkins et al. 2008). The K-S tests on the HR distributions show that the probability for $70\mu\text{m}$ /X-ray galaxies and X-ray selected sample to be drawn from the same population is less than 0.3%. The presence of more X-ray absorption suggests an additional process not accounted for in the conventional AGN unified model scheme.
- (iii) We find that there is no difference between $70\mu\text{m}$ /X-ray galaxies and $70\mu\text{m}$ galaxies in the observed far-infrared colour $\log(F_{70\mu\text{m}}/F_{160\mu\text{m}})$, suggesting the mechanism of far-infrared emission in galaxies could be mainly due to star formation disregarding the presence of AGNs.

ACKNOWLEDGEMENTS

We would like to appreciate the anonymous referee for his/her patience and constructive suggestions and corrections that further improved this paper. We also thank to Richard Davies for the corrections of the English text in my manuscript. The work presented here is supported by the National Science Council of Taiwan under the grants NSC99-2112-M-003-002-MY2, NSC99-2119-M-003-005, and NSC99-2112-M-003-001-MY2. We would like to acknowledge the wonderful work done by Jeyhan S. Kartaltepe on the Spitzer-COSMOS $70\mu\text{m}$ point source catalog on which our analyses are based. We would like to thank the following people for very useful discussions, suggestions, and comments: Lin-

Wen Chen, Jeyhan S. Kartaltepe, Wei-Hao Wang, Albert Kong, Matthew A. Malkan, Nick Scoville, David B. Sanders, Richard Davies, David Rosario, and Dieter Lutz. This research used extensively the COSMOS survey archive data of the NASA/IPAC Infrared Science Archive, which is operated by the Jet Propulsion Laboratory, California Institute of Technology, under contract with the National Aeronautics and Space Administration.

REFERENCES

- Abazajian K. N. et al., 2009, *ApJS*, 182, 543
 Alexander D. M. et al., 2005, *Nature*, 434, 738
 Alonso-Herrero A. et al., 2006, *ApJ*, 640, 167
 Antonucci R., 1993, *ARA&A*, 31, 473
 Armus L., 2006, in Armus L., Reach W.T., eds, *ASP Conf. Ser. Vol. 357, The Spitzer Space Telescope: New Views of the Cosmos*. Astron. Soc. Pac., San Francisco, p. 218
 Arnouts S. et al., 1999, *MNRAS*, 310, 540
 Baldwin J. A., Phillips M. M., & Terlevich R., 1981, *PASP*, 93, 5
 Balestra I., Boller T., Gallo L., Lutz D., & Hess S., 2005, *A&A*, 442, 469
 Barnes J. E., & Hernquist L. E., 1991, *ApJ*, 370, L65
 Bennert N. et al., 2008, *ApJ*, 677, 846
 Biggs A. D., & Ivison R. J., 2008, *MNRAS*, 385, 893
 Borne K. D., Bushouse H., Lucas R. A., & Colina L., 2000, *ApJ*, 529, L77
 Brusa M. et al., 2007, *ApJS*, 172, 353
 Brusa M. et al., 2010, *ApJ*, 716, 348
 Canalizo G., & Stockton A., 2001, *ApJ*, 555, 719
 Capak P. et al., 2007, *ApJS*, 172, 99
 Cappelluti N. et al., 2009, *A&A*, 497, 635
 Casey C. M. et al., 2009, *MNRAS*, 399, 121
 Casey C. M., 2012, *MNRAS*, 425, 3094
 Chapman S. C., Blain A. W., Smail I., & Ivison R. J., 2005, *ApJ*, 622, 772
 Choi P. I. et al., 2011, *ApJ*, 732, 21
 Clements D. L., Dunne L., & Eales S., 2010, *MNRAS*, 403, 274
 Comastri A., 2004, in Barger A. J., ed., *Astrophysics and Space Science Library Vol. 308, Supermassive Black Holes in the Distant Universe*, The Netherlands, p. 245
 Cui J., Xia X.-Y., Deng Z.-G., Mao S., & Zou Z.-L., 2001, *AJ*, 122, 63
 de Grijp M. H. K., Miley G. K., Lub J., & de Jong T., 1985, *Nature*, 314, 240
 Donley J. L., Rieke G. H., Pérez-González P. G., Rigby J. R., & Alonso-Herrero A., 2007, *ApJ*, 660, 167
 Donley J. L., Rieke G. H., Pérez-González P. G., & Barro G., 2008, *ApJ*, 687, 111
 Elbaz D. et al., 2010, *A&A*, 518, L29
 Elvis M. et al., 2009, *ApJS*, 184, 158
 Engel H. et al., 2010, *ApJ*, 724, 223
 Esquej P. et al., 2012, *MNRAS*, 423, 185
 Franceschini A. et al., 2003, *MNRAS*, 343, 1181
 Frayer D. T. et al., 2009, *AJ*, 138, 1261
 Gallagher S. C., Brandt W. N., Chartas G., Garmire G. P., & Sambruna R. M., 2002, *ApJ*, 569, 655
 Gandhi P. et al., 2009, *A&A*, 502, 457
 Genzel R., & Cesarsky C. J., 2000, *ARA&A*, 38, 761
 Genzel R. et al., 1998, *ApJ*, 498, 579
 Gilli R., Comastri A., & Hasinger G., 2007, *A&A*, 463, 79
 Greve T. R. et al., 2005, *MNRAS*, 359, 1165
 Haardt F., & Maraschi L., 1993, *ApJ*, 413, 507
 Hasinger G. et al., 2007, *ApJS*, 172, 29
 Hopkins P. F., Hernquist L., Cox T. J., & Kereš D., 2008, *ApJS*, 175, 356
 Ilbert O. et al., 2006, *A&A*, 457, 841
 Ilbert O. et al., 2009, *ApJ*, 690, 1236
 Imanishi M., Maiolino R., & Nakagawa T., 2010, *ApJ*, 709, 801
 Iono D. et al., 2007, *ApJ*, 659, 283
 Iwasawa K. et al., 2005, *MNRAS*, 357, 565
 Kartaltepe J. S. et al., 2010a, *ApJ*, 709, 572
 Kartaltepe J. S. et al., 2010b, *ApJ*, 721, 98
 Kartaltepe J. S. et al., 2012, *ApJ*, 757, 23
 Kocevski D. D. et al., 2012, *ApJ*, 744, 148
 Koekemoer A. M. et al., 2007, *ApJS*, 172, 196
 Komossa S. et al., 2003, *ApJ*, 582, L15
 Kormendy J., & Richstone D., 1995, *ARA&A*, 33, 581
 Kovács A. et al., 2006, *ApJ*, 650, 592
 Lacy M. et al., 2004, *ApJS*, 154, 166
 Laird E. S., Nandra K., Pope A., & Scott D., 2010, *MNRAS*, 401, 2763
 LaMassa S. M. et al., 2012, *ApJ*, 758, 1
 Lee N. et al., 2010, *ApJ*, 717, 175
 Le Floch E. et al., 2009, *ApJ*, 703, 222
 Lilly S. J. et al., 2007, *ApJS*, 172, 70
 Lusso E. et al., 2013, *ApJ*, 777, 86
 Lutz D., Maiolino R., Spoon H. W. W., & Moorwood A. F. M., 2004, *A&A*, 418, 465
 Magorrian J. et al., 1998, *AJ*, 115, 2285
 Mateos S. et al., 2007, *A&A*, 473, 105
 Merloni A. et al., 2014, *MNRAS*, 437, 3550
 Mullaney J. R., Alexander D. M., Goulding A. D., & Hickox R. C., 2011, *MNRAS*, 414, 1082
 Mullaney J. R. et al., 2012, *MNRAS*, 419, 95
 Netzer H. et al., 2007, *ApJ*, 666, 806
 Patel H., Clements D. L., Rowan-Robinson M., & Vaccari M., 2011, *MNRAS*, 415, 1738
 Polletta M. et al., 2007, *ApJ*, 663, 81
 Pozzi F. et al., 2012, *MNRAS*, 423, 1909
 Prescott M. K. M., Impey C. D., Cool R. J., & Scoville N. Z., 2006, *ApJ*, 644, 100
 Press W. H., Flannery B. P., Teukolsky S. A., & Vetterling W. T., 1992, *Numerical Recipes*, 2nd edition (1992), Chapter 14. Cambridge University Press, Cambridge
 Rafferty D. A. et al., 2011, *ApJ*, 742, 3
 Ranalli P., Comastri A., & Setti G., 2003, *A&A*, 399, 39
 Salvato M. et al., 2009, *ApJ*, 690, 1250
 Sanders D. B., & Mirabel I. F., 1996, *ARA&A*, 34, 749
 Sanders D. B. et al., 1988a, *ApJ*, 325, 74
 Sanders D. B., Soifer B. T., Elias J. H., Neugebauer G., & Matthews K., 1988b, *ApJ*, 328, L35
 Sanders D. B. et al., 2007, *ApJS*, 172, 86
 Schawinski K. et al., 2011, *ApJL*, 727, L31
 Scott K. S. et al., 2008, *MNRAS*, 385, 2225
 Scoville N. et al., 2007a, *ApJS*, 172, 1
 Scoville N. et al., 2007b, *ApJS*, 172, 38
 Shi Y., Rieke G., Lotz J., & Perez-Gonzalez P. G., 2009, *ApJ*, 697, 1764
 Smail I., Swinbank A. M., Ivison R. J., & Ibar E., 2011, *MNRAS*, 414, L95
 Stern D. et al., 2005, *ApJ*, 631, 163
 Symeonidis M. et al., 2010, *MNRAS*, 403, 1474
 Teng S. H., & Veilleux S., 2010, *ApJ*, 725, 1848
 Treister E. et al., 2009, *ApJ*, 706, 535
 Treister E. et al., 2010, *Science*, 328, 600
 Trichas M. et al., 2009, *MNRAS*, 399, 663
 Trump J. R. et al., 2007, *ApJS*, 172, 383
 Tueller J. et al., 2010, *ApJS*, 186, 378
 Ueda Y., Akiyama M., Ohta K., & Miyaji T., 2003, *ApJ*, 598, 886
 Ueda Y., Akiyama M., Hasinger G., Miyaji T., & Watson M. G. 2014, *ApJ*, 786, 104
 Veilleux S., 2002, in Green R.F., Khachikian E.Ye., and Sanders D.B., eds, *ASP Conf. Proc. Vol. 284, AGN Surveys*. Astron. Soc. Pac., San Francisco, p. 111
 Veilleux S., Kim D.-C., & Sanders D. B., 2002, *ApJS*, 143, 315
 Veilleux S. et al., 2009, *ApJS*, 182, 62
 Vignati P. et al., 1999, *A&A*, 349, L57
 Voit G. M., 1992, *MNRAS*, 258, 841
 Wang W.-H., Cowie L. L., Barger A. J., Keenan R. C., & Ting H.-C., 2010, *ApJS*, 187, 251
 Weedman D. W. et al., 2005, *ApJ*, 633, 706
 Wilkes B. J. et al., 2005, *ApJ*, 634, 183

Yang M., Greve T. R., Dowell C. D., & Borys C., 2007, ApJ, 660, 1198